Stability of VOF Method under High-Order Convective Discretization for Breaking Waves

S.P. Yoon[1], G. Go[2], D. Seo[2], S. Brizzolara[3] and H.T. Ahn[1,*]
Corresponding author[*]: htahn@ulsan.ac.kr
[1] School of Naval Architecture and Ocean Engineering, University of Ulsan, South Korea.
[2] Hyundai Maritime Research Institute, HD Hyundai Heavy Industries, South Korea.
[3] Kevin T. Crofton Department of Aerospace and Ocean Engineering, Virginia Tech, Blacksburg, VA, USA.

Abstract: Wave breaking is a strongly nonlinear free-surface problem involving interface overturning, jet formation and impact, air entrainment, and topological change, and it constitutes a stringent test of the coupling between interface capturing and momentum-convection discretization. High-order convective schemes resolve nonlinear transport with low numerical dissipation, but the same low dissipation may permit nonphysical oscillations near the interface that threaten the robustness of algebraic volume-of-fluid transport. This study examines whether an algebraic VOF framework, based on a tangent-of-hyperbola interface-capturing formulation, can robustly capture strongly nonlinear breaking-wave dynamics when coupled with high-order convection. Within an otherwise identical projection-based incompressible solver, only the momentum-convection discretization is varied across the first-order upwind, MUSCL, WENO-JS, WENO-Z, and TENO schemes, isolating the role of scheme-dependent dissipation. Two-dimensional simulations are performed at a wave steepness of 0.55, and three-dimensional extensions examine spilling and plunging breaking features. The schemes are compared through the free-surface evolution and the time history of the normalized wave energy. The first-order upwind scheme delays the breaking onset, whereas the high-resolution schemes follow nearly indistinguishable energy-decay histories and reproduce the energy-decay trend of the reference data, differing only in local interface morphology, with TENO resolving the thinnest jet and the finest fragments. The results indicate that the algebraic transport remains bounded and non-oscillatory during severe jet impact and air entrainment across all schemes, so that scheme-dependent dissipation governs the local interface morphology rather than the global stability of the coupled framework.

Keywords: Breaking Wave, Computational Fluid Dynamics, Free-surface Flow, Hydrodynamics.

1. Introduction

In the operation of ships and offshore structures, complex free-surface phenomena such as sloshing, slamming, and green water occur frequently and directly affect structural safety and operational performance. These phenomena arise in air–water two-phase flows with density and viscosity changing abruptly across the interface separating the two fluids. The large density and viscosity ratios between water and air introduce sharp discontinuities in fluid properties across the interface and heighten the sensitivity of the numerical solution to the position and shape of the free surface. Because strong nonlinear behavior such as large interfacial deformation, wave overturning and breaking, jet formation, and air entrainment is involved as well, a stable and accurate prediction of the temporal and spatial evolution of the free surface is essential for reliable hydrodynamic load estimation and flow-field analysis.

The performance assessment of marine systems requires analysis over a wide range of sea states, operating conditions, and geometric configurations. Comprehensive experimental testing under all relevant conditions is often impractical because of limitations in experimental facilities, scale effects, measurement uncertainty, and high cost. Computational fluid dynamics provides an effective means of repeatedly analyzing complex free-surface flows under controlled conditions and offers detailed information on interfacial behavior and local flow structures that are difficult to obtain experimentally. Accordingly, the robust coupling of an interface-capturing method for describing free-surface transport and deformation with a spatial discretization scheme capable of resolving nonlinear convection is of central importance.

Wave breaking is a representative strongly nonlinear free-surface problem in which interface overturning, jet formation and impact, air entrainment, and topological changes of the free surface occur in combination. It therefore provides a challenging benchmark problem for evaluating both the robustness of an interface-capturing method and the resolution characteristics of a momentum-convection discretization scheme. High-order convective discretization generally provides improved resolution of wave propagation and local flow structures because of its relatively low numerical dissipation. Reduced numerical dissipation may, however, permit nonphysical oscillations to develop in the velocity and pressure fields near the interface. These oscillations can, in turn, compromise the robustness of the coupled algebraic volume-of-fluid (VOF) transport during wave breaking involving large interfacial deformation. Conversely, excessive numerical dissipation may improve computational robustness but can also increase wave attenuation and interface smearing, thereby degrading the prediction of breaking onset and free-surface geometry. The principal challenge is therefore not simply to minimize numerical dissipation, but to retain low-dissipation accuracy while maintaining non-oscillatory interface transport.

Interface-capturing within the VOF framework is broadly realized through either geometric reconstruction, in which the interface is explicitly recovered within each cell [1] [2] [3], or algebraic transport, in which the interfacial flux is evaluated directly from the discrete volume-fraction field without geometric reconstruction. Motivated by these considerations, the present study employs an algebraic VOF method, specifically a tangent-of-hyperbola interface-capturing (THINC) formulation [4] and investigates how its coupling with different momentum-convection discretization schemes affects the numerical stability and fidelity of free-surface prediction in strongly nonlinear breaking-wave simulations.

To isolate the influence of the momentum-convection discretization, all other components of the projection-based incompressible flow solver are retained, and only the convective scheme is varied. The schemes considered range from low-order upwind formulations to high-resolution methods belonging to the essentially non-oscillatory family and differ in both formal order of accuracy and numerical-dissipation characteristics. The computations are conducted using the same grid resolution and Courant-number criterion, allowing the observed differences to be attributed primarily to the convective discretization rather than to the time-integration or pressure-projection procedure. The comparison focuses on the global evolution of the free surface and the associated flow field during wave breaking, from which the role of scheme-dependent numerical dissipation in the stability of the coupled algebraic VOF framework is assessed. A comparative study of geometric reconstruction-based VOF methods is reserved for future work.

2. Numerical Methodology

2.1. Governing equations for incompressible flow

Both water and air are modeled as incompressible Newtonian fluids within a one-fluid formulation. The governing equations are the incompressible Navier–Stokes equations with gravitational acceleration [5]. The continuity and momentum equations are written as

$$\frac{\partial \boldsymbol{U}}{\partial t} + (\boldsymbol{U} \cdot \nabla)\boldsymbol{U} = -\frac{1}{\rho}\nabla p + \frac{1}{\rho}\nabla \cdot [\mu(\nabla \boldsymbol{U} + \nabla \boldsymbol{U}^{\mathrm{T}})] + \boldsymbol{g}$$

$$\nabla \cdot \boldsymbol{U} = 0$$

where $\boldsymbol{U}$ is velocity vector, p is the pressure, $\boldsymbol{g}$ is the gravitational acceleration, t is time, ρ is density and μ is dynamic viscosity. Within the one-fluid formulation, density and viscosity are defined as functions of the volume fraction χ and are incorporated into the momentum equation.

2.2. Projection method for pressure-velocity coupling

The numerical solution is obtained using a projection-based incompressible flow solver based on an established incremental pressure-correction framework [6, 7]. The solution procedure consists of predictor, projection, and corrector stages. In the predictor stage, an intermediate velocity $\boldsymbol{U}^*$ is computed without imposing the divergence-free constraint.

$$\boldsymbol{U}^* = \boldsymbol{U}^n + \Delta t\left(\frac{3}{2}\boldsymbol{F}^n - \frac{1}{2}\boldsymbol{F}^{n-1}\right) - \frac{\Delta t}{\rho}\nabla p^n$$

where $\boldsymbol{F}(\boldsymbol{U}) = -(\boldsymbol{U} \cdot \nabla)\boldsymbol{U} + \frac{1}{\rho}\nabla \cdot [\nu(\nabla \boldsymbol{U} + \nabla \boldsymbol{U}^{\mathrm{T}})] + \boldsymbol{g}$ represents the convective, diffusive, and gravitational contributions. These terms are evaluated explicitly using the second-order Adams–Bashforth scheme, while the pressure gradient from the previous time level is retained in accordance with the incremental pressure-correction formulation. The superscripts $n-1$, n, and $n+1$ denote the previous, current, and next time levels, respectively. In the present study, only the spatial discretization of the momentum-convection term is varied, whereas the temporal discretization, viscous operator, body-force treatment, VOF transport formulation, and pressure-correction procedure are maintained identically for all configurations

In the projection stage, the intermediate velocity is decomposed into solenoidal and irrotational components subject to the prescribed boundary conditions. The irrotational component is represented by the gradient of a pressure increment δp. Enforcing the incompressibility condition on the corrected velocity yields the following variable-coefficient pressure Poisson equation.

$$\nabla \cdot \left[\frac{1}{\rho}\nabla(\delta p)\right] = \frac{1}{\Delta t}\nabla \cdot \boldsymbol{U}^*$$

The coefficient $\frac{1}{\rho}$ accounts for the discontinuous density distribution represented by the volume-fraction field. The pressure increment is determined subject to the prescribed pressure boundary conditions and an appropriate pressure reference.

In the corrector stage, the divergence-free velocity and the pressure at the new time level are obtained as

$$\boldsymbol{U}^{n+1} = \boldsymbol{U}^* - \frac{\Delta t}{\rho}\nabla(\delta p)$$

$$p^{n+1} = p^n + \delta p$$

The corrected velocity satisfies the discrete continuity equation to the convergence tolerance of the pressure Poisson solver. Because all these components are held fixed, differences in the computed free-surface evolution can be attributed primarily to the formal accuracy and numerical-dissipation characteristics of the convective schemes considered.

2.3. Spatial discretization of convective term

In this study, the convective term is discretized in advective form, and five schemes differing in stencil width and weighting strategy for face-value reconstruction are adopted for comparison: the first-order upwind scheme, the monotonic upstream-centered scheme for conservation laws (MUSCL) [8], and two members of the essentially non-oscillatory (ENO) family, namely the weighted ENO (WENO) [9, 10] and targeted ENO (TENO) [11] schemes . The WENO scheme is further evaluated in two distinct variants, the WENO5-JS scheme of Jiang and Shu and the WENO5-Z scheme of Borges et al.

All schemes share a common framework in which the derivative is evaluated by face differencing after the face value has been reconstructed. The advective form of the convective term is expressed as

$$(\boldsymbol{U}\cdot\nabla)\boldsymbol{U} = \left(u\frac{\partial u}{\partial x}\bigg|_{ij} + v\frac{\partial u}{\partial y}\bigg|_{ij}, u\frac{\partial v}{\partial x}\bigg|_{ij} + v\frac{\partial v}{\partial y}\bigg|_{ij} \right)$$

where the subscripts denote the cell index. Each one-dimensional derivative is computed in face-difference form, and the scheme dependence enters only through the face-value reconstruction,

$$\frac{\partial \phi}{\partial x}\bigg|_i = \frac{\phi_{i+0.5} - \phi_{i-0.5}}{\Delta x}$$

where ϕ is the reconstructed variable and $\phi_{i\pm1/2}$ are the face values reconstructed at the cell interfaces. The differences among the schemes in this study originate entirely from these reconstructed face values.

2.3.1. 1st-order upwind scheme

The sign of the advection velocity determines the upwind bias, where $a$denotes the advecting velocity along the differentiation direction. Accordingly, the first-order upwind scheme employs a one-sided difference selected by the sign of the advection velocity,

$$\frac{\partial \phi}{\partial x}\bigg|_i = \begin{cases} (\phi_i - \phi_{i-1})/\Delta x, & a \geq 0 \\ (\phi_{i+1} - \phi_i)/\Delta x, & a < 0 \end{cases}$$

The first-order upwind scheme is the simplest and most robust, but its large numerical diffusion excessively smears vorticity and fine-scale structures; it is therefore employed only as a baseline against which the behavior of the higher-order schemes is gauged.

2.3.2. MUSCL scheme

The MUSCL scheme reconstructs the face values from limited slopes. Denoting the differences between adjacent cells by d^- and d^+, the van Leer limiter is defined as

$$\sigma(d^-, d^+) = \begin{cases} 2d^-d^+/(d^- + d^+), & d^-d^+ > 0 \\ 0, & d^-d^+ \leq 0 \end{cases}$$

where d^- and d^+ are the backward and forward differences relative to the reconstruction point, respectively, and the limiter vanishes at extrema where the two differences have opposite signs. For a positive advecting velocity, the face values are reconstructed in a left-biased manner as

$$\phi_{i-0.5} = \phi_{i-1} + \frac{1}{2}\sigma(\phi_{i-1} - \phi_{i-2}, \phi_i - \phi_{i-1})$$
$$\phi_{i+0.5} = \phi_i + \frac{1}{2}\sigma(\phi_i - \phi_{i-1}, \phi_{i+1} - \phi_i)$$

The limiter restricts the slope in non-monotone regions to suppress the generation of new local extrema, while providing a second-order accurate reconstruction in smooth, monotone regions [8].

2.3.3. ENO-family schemes

The ENO-family schemes go beyond the second-order limit of MUSCL, attaining high-order accuracy in smooth regions while capturing discontinuities in a non-oscillatory manner. Both the WENO and TENO schemes employed in this study divide a five-point stencil into three three-point sub-stencils, construct a candidate polynomial p_k on each sub-stencil, and reconstruct the face value by combining these candidates through nonlinear weights α_k based on the smoothness indicators β_k. The sub-stencil partition S_0, S_1, S_2 for a positive advection velocity is shown in Figure 1; for a negative advecting velocity, this arrangement is mirrored symmetrically about the interface $i + 1/2$.

$$\phi_{i+0.5} = \frac{\sum_k \alpha_k p_k}{\sum_k \alpha_k}$$

Here $k = 0, 1, 2$ is the sub-stencil index, p_k is the candidate reconstruction constructed on each sub-stencil, and β_k is the smoothness indicator of each sub-stencil, taking smaller values where the solution is smoother in the corresponding region. The three methods use identical candidate sub-stencils but differ in the nonlinear combination or selection strategy that determines the contribution of each sub-stencil, and this difference governs the order preservation in smooth regions and the dissipation characteristics near discontinuities.

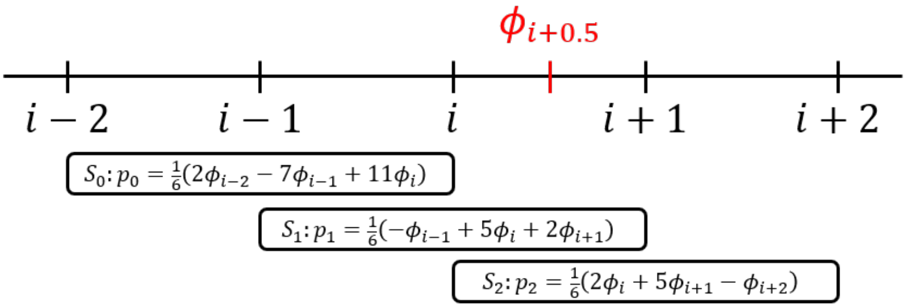

Figure 1: Stencil arrangement employed in the face-value reconstruction of $\phi_{i+1/2}$ for the WENO and TENO schemes when the advection velocity is positive ($a \geq 0$). The five-point stencil is divided into three-point sub-stencils S_0, S_1, and S_2.

The WENO5-JS scheme employs weights inversely proportional to the square of the smoothness indicators,

$$\alpha_k = \frac{d_k}{(\beta_k + \varepsilon)^2}$$

where d_k is the ideal weight that yields the optimal order of accuracy and $\varepsilon$is a small positive constant that prevents the denominator from vanishing. By strongly suppressing the weight of sub-stencils containing discontinuities, the scheme secures non-oscillatory behaviour; however, it suffers from order degradation at smooth extrema and exhibits somewhat dissipative behavior [10].

The WENO5-Z scheme introduces a global smoothness measure $\tau_5 = \mid \beta_0 - \beta_2 \mid$, defined as the difference between the smoothness indicators of the outermost sub-stencils, and redefines the weights as

$$\alpha_k = d_k \left[1 + \left(\frac{\tau_5}{\beta_k + \varepsilon} \right)^2 \right]$$

By incorporating the global measure τ_5, the nonlinear weights are restored closer to the ideal weights in smooth regions, providing lower dissipation and higher resolution than the WENO5-JS scheme. This is advantageous for preserving the wave profile and vorticity prior to wave breaking [9].

The TENO5 scheme evaluates a normalized smoothness measure φ_k for each sub-stencil and then determines its acceptance in a binary manner by comparison with a threshold C_T,

$$\gamma_k = \left(1 + \frac{\tau_5}{\beta_k + \varepsilon} \right)^6, \varphi_k = \frac{\gamma_k}{\sum_m \gamma_m}$$

where γ_k is the unnormalized measure of each sub-stencil, φ_k is its value normalized by the total sum, and m is the summation index for the normalization. Sub-stencils whose computed φ_k falls below the threshold C_T are entirely discarded, while the surviving sub-stencils are assigned the ideal weights directly,

$$\alpha_k = \begin{cases} 0, & \varphi_k < C_T \\ d_k, & \varphi_k \geq C_T \end{cases}$$

where C_T is the threshold that determines the acceptance of each sub-stencil. In smooth regions, all sub-stencils are retained so that the optimal order is preserved, whereas near discontinuities the contaminated stencils are blocked in a binary fashion, thereby achieving both low dissipation and sharp discontinuity capture [11].

2.4. Interface capturing for free-surface flow

The air–water interface is captured using the volume-of-fluid (VOF) method, in which the volume fraction χ represents the fractional occupancy of liquid within each computational cell and is advected by the underlying velocity field. Under the one-fluid assumption, χ varies between zero in the gas phase and unity in the liquid phase, and its transport is governed by

$$\frac{\partial \chi}{\partial t} + \nabla \cdot (\chi \boldsymbol{U}) = 0$$

where $\boldsymbol{U}$ is the velocity field shared by both phases. The fluid properties, namely density ρ and dynamic viscosity μ, are evaluated as functions of χ, so that the interface location is reflected directly in the property fields entering the momentum equation.

The present study adopts an algebraic interface-capturing approach based on the tangent-of-hyperbola interface capturing concept [4], in which the interfacial transition is represented by a smoothed hyperbolic-tangent profile across the interface. This formulation maintains a sharp yet bound interface, suppressing the numerical diffusion that would otherwise smear the volume fraction while preserving the boundedness $0 \leq \chi \leq 1$ required for physically admissible interfaces. The compressive nature of the reconstruction counteracts interface smearing under advection, which is essential for resolving the thin jets and entrained-air structures that characterize breaking waves.

3. Results

The wave steepness is defined as $\varepsilon = ka$, where k is the wavenumber and a is the amplitude. Two conditions, $\varepsilon = 0.35$ and $\varepsilon = 0.55$, were considered in this study. The two-dimensional simulations were performed on a unit square domain with a uniform grid resolution of 256×256 and a fixed time step of $\Delta t = 10^{-4}$. The initial condition was prescribed as a third-order Stokes wave, following the breaking configuration of Chen et al. [12]. Throughout the computation the Courant–Friedrichs–Lewy condition was monitored at every time step to ensure that the stability criterion was strictly satisfied.

The free-surface evolution is assessed through two complementary measures: instantaneous snapshots of the interface and the time history of the total wave energy. The total energy E is defined as the sum of the kinetic and potential contributions integrated over the domain, where the potential energy is referenced to the mean water level and excludes the hydrostatic component, so that E represents the wave energy associated with free-surface deformation rather than the resting hydrostatic state. The energy is normalized by its initial value E_0, and the time is normalized by the wave period T.

The snapshot sequence resolves the canonical plunging-breaker cascade. The wave crest first steepens and develops pronounced fore-aft asymmetry; under gravity the overhanging crest is drawn downward, forming a thin forward jet that overturns and plunges onto the forward face of the wave. The plunging impact reconfigures the interface and encloses an air pocket, which is subsequently advected and fragmented downstream as entrained air.

A close comparison of the snapshot sequences shows that the first-order upwind scheme develops the breaking process at a visibly different rate, owing to its excessive numerical diffusion, so that its snapshots do not correspond to the same developmental stage as the higher-order schemes. The MUSCL, WENO-JS, WENO-Z, and TENO schemes, in contrast, evolve in close synchrony, and the snapshots in Figures 3–6 are therefore presented at matched instants to enable a direct stage-by-stage comparison. At these matched instants the TENO scheme retains a thinner jet tip and resolves finer detached liquid fragments and entrained-air structures than the WENO variants. This sharper resolution of thin interfacial features is consistent with the lower numerical dissipation of TENO, which discards only contaminated sub-stencils while assigning ideal weights to the remainder. A definitive accuracy ranking among the high-resolution schemes would require a converged reference solution and a quantitative interface metric and is therefore deferred to future work.

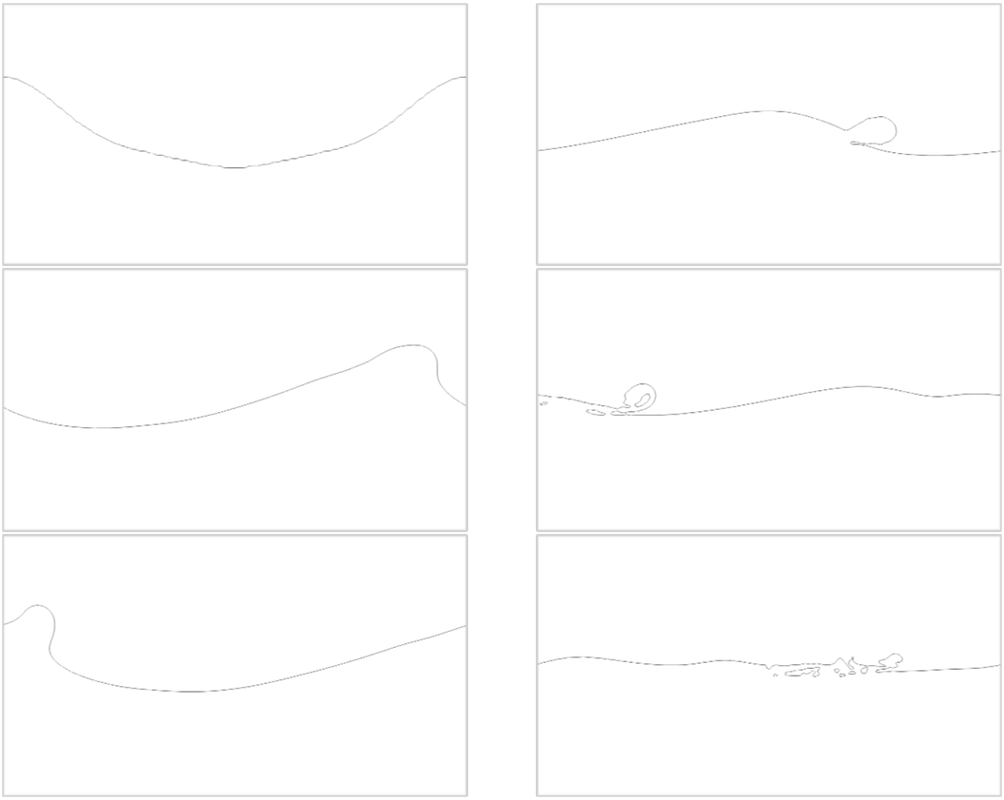

Figure 2: Free-surface evolution at wave steepness obtained with the first-order upwind scheme

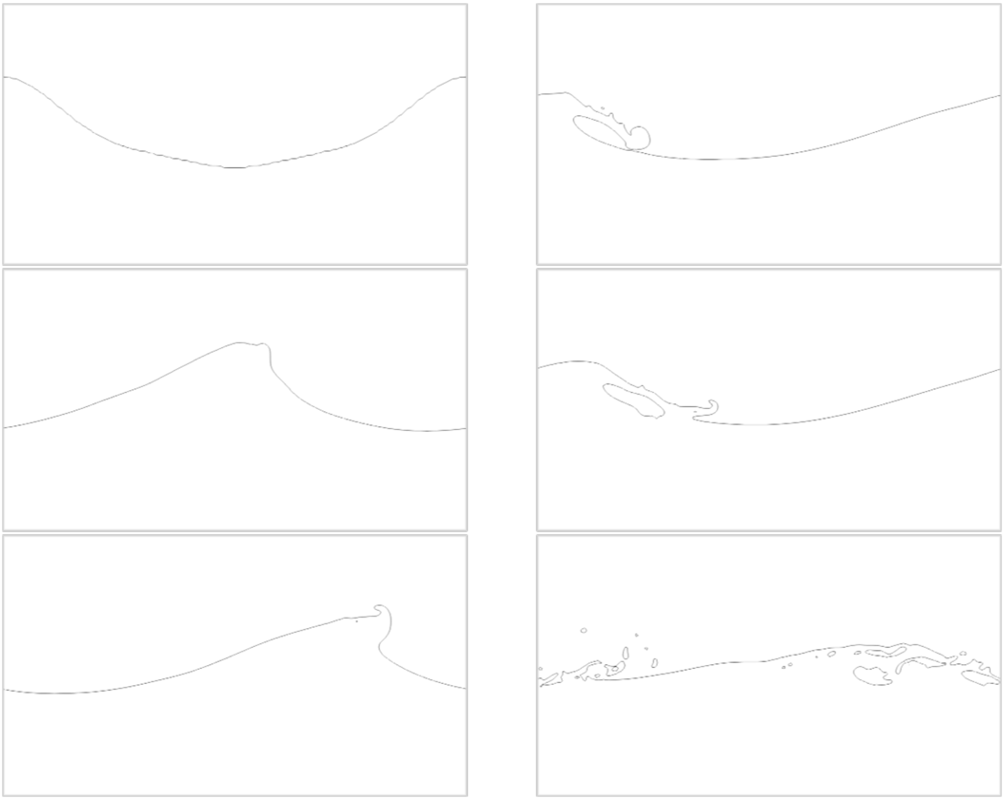

Figure 3: Free-surface evolution at wave steepness obtained with the MUSCL scheme

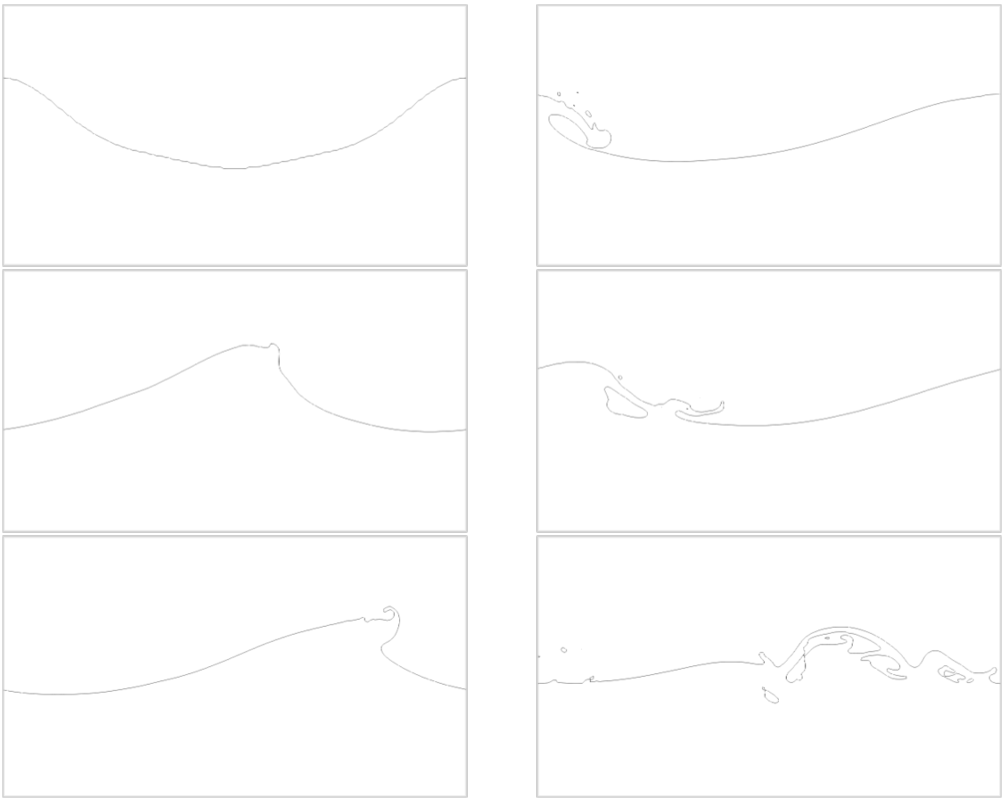

Figure 4: Free-surface evolution at wave steepness obtained with the WENO-JS scheme

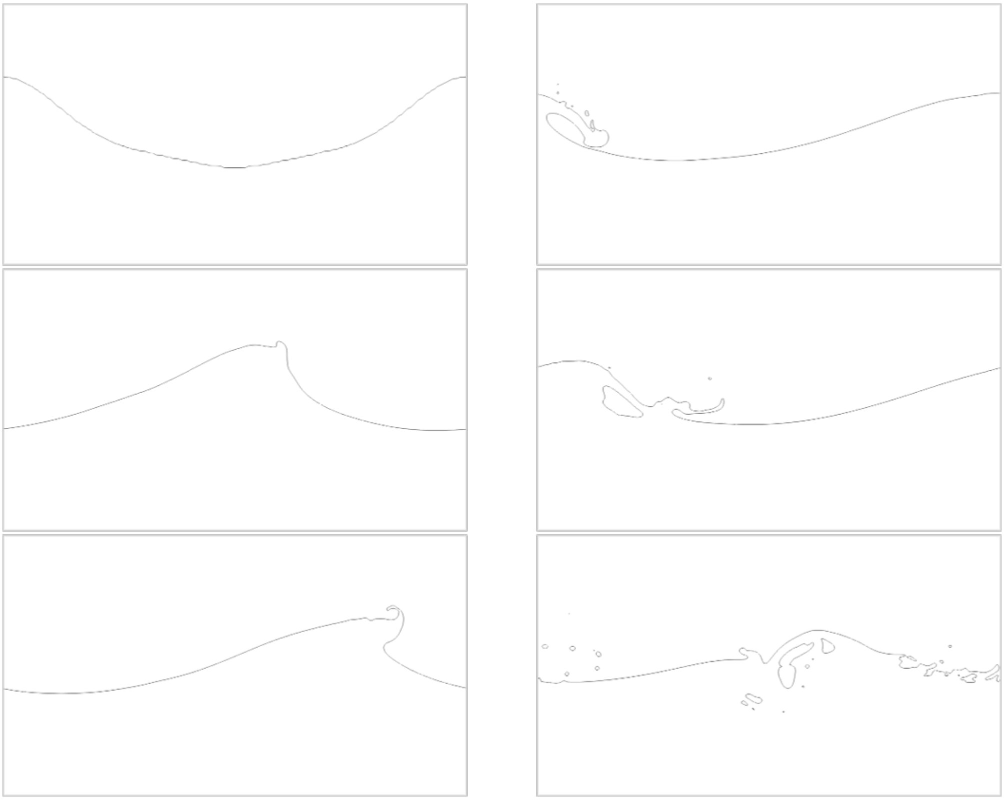

Figure 5: Free-surface evolution at wave steepness obtained with the WENO-Z scheme

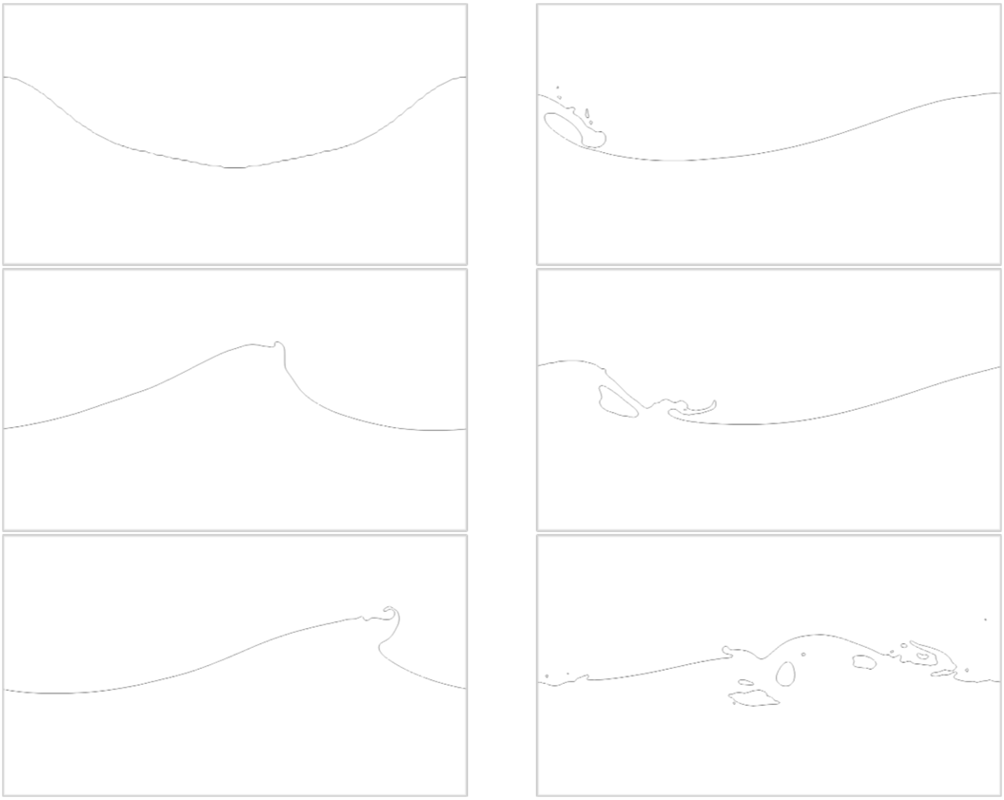

Figure 6: Free-surface evolution at wave steepness obtained with the TENO scheme

Figure 7 reports the normalized wave energy E/E_0 against t/T for the five convective schemes, together with the reference data of Chen et al. [12]. The first-order upwind scheme retains energy longest and exhibits a delayed transition into the rapid-dissipation phase, a direct consequence of its excessive numerical diffusion, which smears the crest and postpones the onset of overturning. The MUSCL and essentially non-oscillatory schemes collapse onto a tightly clustered band, indicating that once the convective discretization is sufficiently low in dissipation the global energy budget becomes largely insensitive to the specific high-resolution reconstruction. The WENO-JS, WENO-Z, and TENO schemes, which share the same formal order, follow nearly indistinguishable decay histories; the integral energy metric does not by itself separate one high-resolution scheme from another, and their differences instead emerge in the local interface morphology examined above. The high-resolution schemes reproduce the energy-decay trend of Chen et al. [12], including the onset of the rapid-dissipation phase, although the present results decay somewhat more slowly at the coarser resolution, which is attributable to the reduced grid resolution rather than to the convective discretization. This agreement confirms that algebraic transport does not introduce excessive artificial dissipation under high-order convection.

As shown in Figure 8, in the three-dimensional extended simulations, the primary wave breaking mechanisms observed in two dimensions were maintained, but additional spatial complexity emerged due to spanwise modulation. A spilling breaker profile was observed at $\varepsilon = 0.35$, whereas a plunging breaker profile was dominant at $\varepsilon = 0.55$. Notably, the location of the jet impact and the distribution of the entrained air were highly nonuniform in the spanwise direction, underscoring the critical importance of three-dimensional effects in breaking wave dynamics.

Despite the use of a high-order low-dissipative scheme, the algebraic VOF framework maintained stable interface evolution throughout severe jet impact and air entrainment phases. No numerical instability or unphysical oscillation was observed during rapid topological transitions. This indicates that the algebraic transport and sharpening mechanism provide sufficient robustness against the reduced numerical dissipation introduced by the high-order scheme.

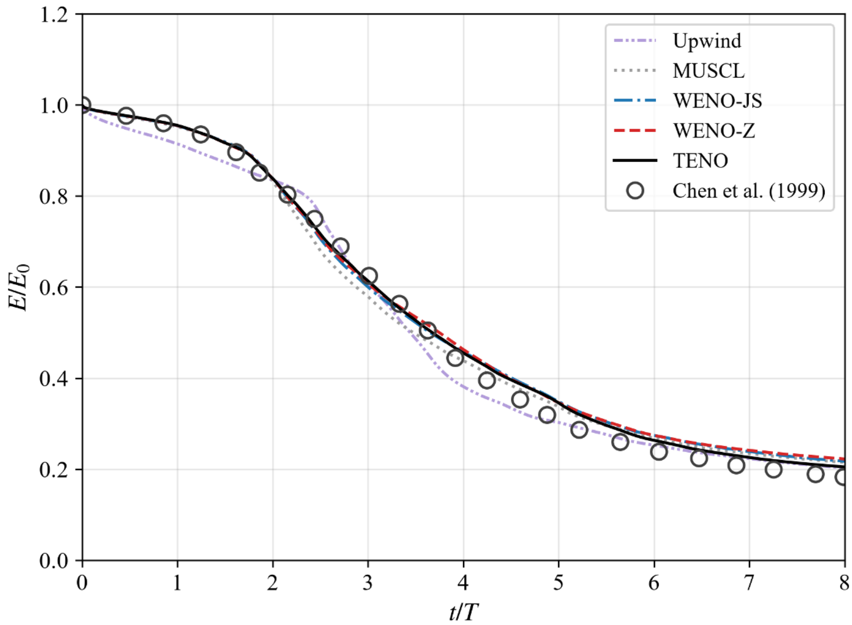

Figure 7: Time history of the normalized wave energy

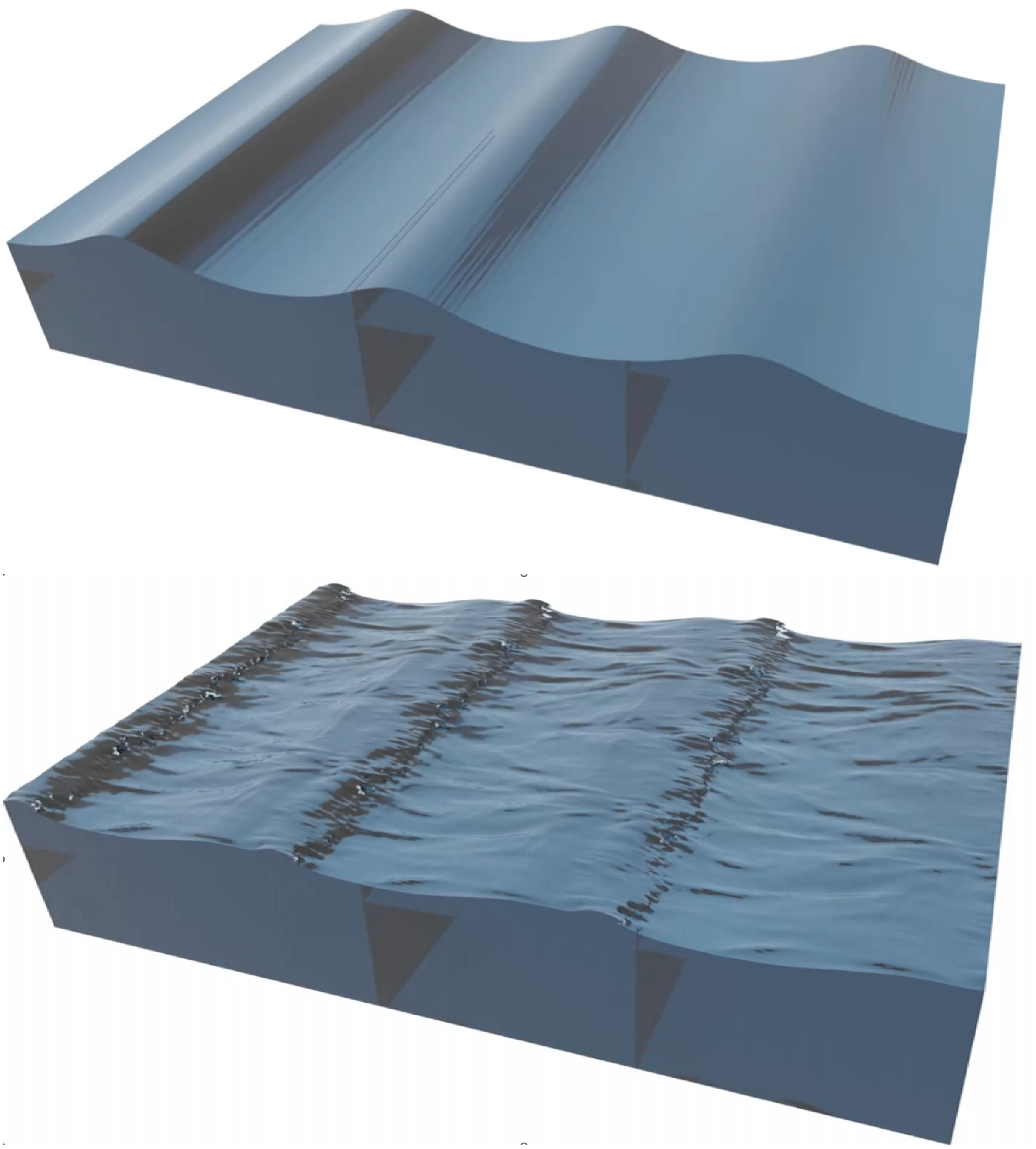

Figure 8: Free-surface evolution for wave steepness of 0.35

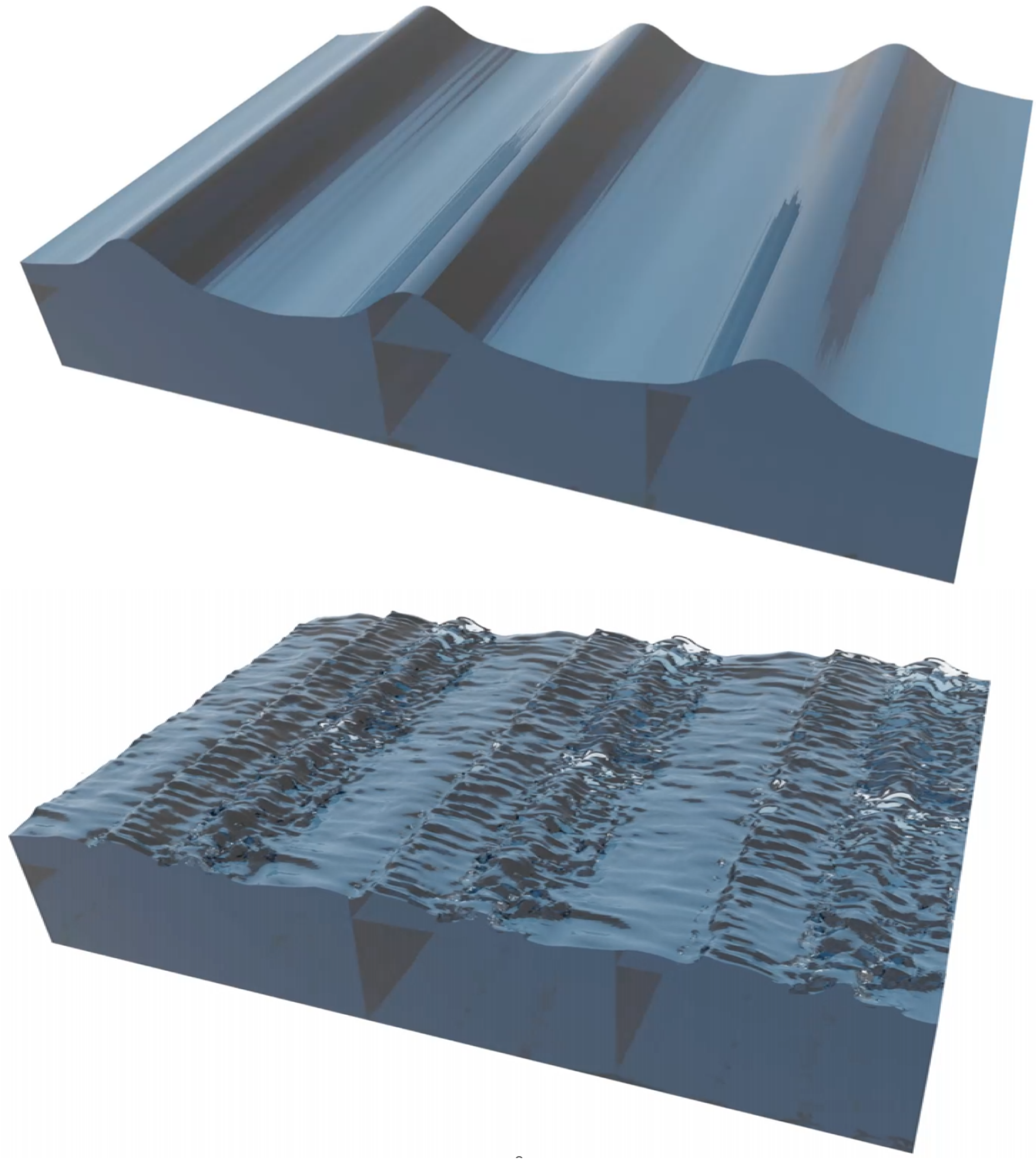

Figure 9: Free-surface evolution for wave steepness of 0.55

4. Conclusion and Future Work

This study assessed how the choice of momentum-convection discretization affects the stability and fidelity of an algebraic VOF framework under strongly nonlinear wave breaking, comparing the first-order upwind, MUSCL, WENO-JS, WENO-Z, and TENO schemes within an otherwise identical projection-based incompressible solver. A breaking wave problem, characterized by strong nonlinear transport and massive topological changes, was selected as the validation benchmark to compare the free-surface deformation and the energy-dissipation behavior across the schemes and across wave steepness conditions.

The first-order upwind scheme delayed the onset of overturning owing to its excessive numerical diffusion, whereas the high-resolution schemes reproduced the crest-steepening, overturning, thin-jet, and air-entrainment cascade and collapsed onto a tightly clustered energy-decay band. The normalized wave energy reproduced the decay trend and the onset of the rapid-dissipation phase with the residual difference attributable to the coarser grid resolution rather than to the convective discretization. The integral energy metric did not separate one high-resolution scheme from another; their differences emerged only in the local interface morphology, where TENO retained the thinnest jet and the finest detached fragments, consistent with its lower numerical dissipation. Across all schemes the algebraic transport remained bounded and non-oscillatory through severe jet impact and air entrainment, confirming that the compressive interface reconstruction provides sufficient robustness against the reduced dissipation of high-order convection.

Future research will apply a geometric reconstruction-based VOF method to conduct additional evaluations, including a direct comparison with the geometric approach under identical breaking conditions. Through this, we aim to expand the applicable range of the present numerical procedure in terms of interface fidelity, numerical stability, and sensitivity to numerical setups, ultimately providing more reliable computational guidelines for free surface breaking wave problems.

Acknowledgements

This research was partly supported by the Regional Innovation System & Education (RISE) program through the Ulsan RISE Center, funded by the Ministry of Education (MOE) and the Ulsan Metropolitan City, Republic of Korea (2026-RISE-07-001), and by the Korea Research Institute for Defense Technology Planning and Advancement (KRIT) grant funded by the Defense Acquisition Program Administration (DAPA) (KRIT-CT-22-066).

References

[1] H. T. Ahn and M. Shashkov, "Multi-material interface reconstruction on generalized polyhedral meshes," *J. Comput. Phys.,* vol. 226, no. 2, pp. 2096-2132, 2007.

[2] H. T. Ahn and M. Shashkov, "Adaptive moment-of-fluid method," *J. Comput. Phys.,* vol. 228, no. 8, pp. 2792-2821, 2009.

[3] H. T. Ahn, M. Shashkov and M. A. Christon, "The moment-of-fluid method in action," *Commun. Numer. Methods Eng.,* vol. 25, no. 10, pp. 1009-1018, 2009.

[4] K. Yokoi, "Efficient implementation of THINC scheme: A simple and practical smoothed VOF algorithm," *J. Comput. Phys.,* vol. 226, no. 2, pp. 1985-2002, 2007.

[5] Y. Kallinderis and H. T. Ahn, "Incompressible Navier-Stokes method with general hybrid meshes," *J. Comput. Phys,* vol. 210, no. 1, pp. 75-108, 2005.

[6] T. Q. Nguyen, H. T. Ahn and C. Kavouklis, "High-Order WENO-based Semi-Implicit Projection Method for Incompressible Turbulent Flows: Development, Accuracy, and Reynolds Number Effects," *Int. J. Comput. Fluid Dyn.,* vol. 37, no. 4, pp. 251-278, 2023.

[7] G. Go and H. T. Ahn, "A geometric multigrid accelerated incompressible flow simulation over complex geometries," *Comput. Fluids,* vol. 197, p. 104350, 2020.

[8] B. van Leer, "Towards the ultimate conservative difference scheme. V. A second-order sequel to Godunov's method," *J. Comput. Phys.,* vol. 32, no. 1, pp. 101-136, 1979.

[9] R. Borges, M. Carmona, B. Costa and W. S. Don, "An improved weighted essentially non-oscillatory scheme for hyperbolic conservation laws," *J. Comput. Phys.,* vol. 227, no. 6, pp. 3191-3211, 2008.

[10] G.-S. Jiang and C.-W. Shu, "Efficient implementation of weighted ENO schemes," *J. Comput. Phys.,* vol. 126, no. 1, pp. 202-228, 1996.

[11] L. Fu, X. Y. Hu and N. A. Adams, "A family of high-order targeted ENO schemes for compressible-fluid simulations," *J. Comput. Phys.,* vol. 305, pp. 333-359, 2016.

[12] G. Chen, C. Kharif, S. Zaleski and J. Li, "Two-dimensional Navier-Stokes simulation of breaking waves," *Phys. Fluids,* vol. 11, no. 1, pp. 121-133, 1999.